Synsint Research Group

Available online at www.synsint.com

Synthesis and Sintering

ISSN 2564-0186 (Print), **ISSN** 2564-0194 (Online)

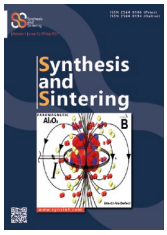

Research article

Role of Ti_3AlC_2 MAX phase on characteristics of in-situ synthesized TiAl intermetallics. Part I: sintering and densification

Maryam Akhlaghi [a], **Esmaeil Salahi** [b,*], **Seyed Ali Tayebifard** [c], **Gert Schmidt** [d]

[a] *Central Reference Laboratory, Iran University of Science and Technology, Narmak, Tehran, 16844, Iran*
[b] *Ceramics Department, Materials and Energy Research Center (MERC), Karaj, Iran*
[c] *Semiconductors Department, Materials and Energy Research Center (MERC), Karaj, Iran*
[d] *Faculty of Mechanical, Process and Energy Engineering, TU Bergakademie, Freiberg, Germany*

A B S T R A C T

Five TiAl–Ti_3AlC_2 composite samples containing (10, 15, 20, 25 and 30 wt% Ti_3AlC_2 MAX phase) were prepared by spark plasma sintering technique at 900 °C for 7 min under 40 MPa. For this purpose, metallic titanium and aluminum powders (aiming at the in-situ formation of the TiAl matrix phase) were ball-milled with predetermined contents of Ti_3AlC_2 MAX phase, which already was synthesized using the same metallic powders as well as graphite flakes. Displacement-time-temperature variations during the heating and sintering steps, displacement rate versus temperature, displacement rate versus time, and densification behavior were studied. Two sharp changes were detected in the diagrams: the first one, ~16 min after the start of the heating process due to the melting of Al, and the second one, after ~35 min because of the sintering progression and the applied final pressure. The highest relative densities were measured for the samples doped with 20 and 25 wt% Ti_3AlC_2 additives. More Ti_3AlC_2 addition resulted in decreased relative density because of the agglomeration of MAX phase particles.

KEYWORDS

In-situ TiAl
Ti_3AlC_2 MAX phase
Spark plasma sintering
DTT graphs
Densification

OPEN ACCESS

1. Introduction

Titanium aluminides are excellent materials for structural applications such as automobile and aerospace industries because of their exceptional combination of characteristics [1–3]. TiAl has low density, high melting point, good corrosion resistance, excellent oxidation performance, and creep resistance [4–6]. Anyway, this intermetallic material suffers from low-temperature ductility and poor formability [7–10]. Spark plasma sintering (SPS) has been used to overcome the poor low-temperature ductility of TiAl. Compared to the conventional powder metallurgical methods, SPS has many benefits such as control of sintering parameters, functional simplicity, high sintering speed, and good reproducibility which helps to obtain contaminant-free, homogeneous, and grain refined microstructures [11–16].

By the introduction of some metallic additive such as Co and Fe, the ductility of TiAl increased via the replacement of aluminum sites with the added metal atoms. Nevertheless, the ductility of TiAl decreased by the addition of Ni, because another intermetallic phase of NiTi is formed at the grain boundaries [17]. TiAl material with enhanced compression properties was obtained by spark plasma sintering using excessive yttrium additive, which led to the formation and dispersion of fine strip-like YAl_2 particles [18]. High-temperature oxidation resistance of TiAl was improved by the addition of Nb or Ta, which support the formation of protective Al_2O_3 non-porous layer [19]. Low

* Corresponding author. *E-mail address:* e-salahi@merc.ac.ir (E. Salahi)
Received 4 September 2021; Received in revised form 25 September 2021; Accepted 26 September 2021.

https://doi.org/10.53063/synsint.2021.1347

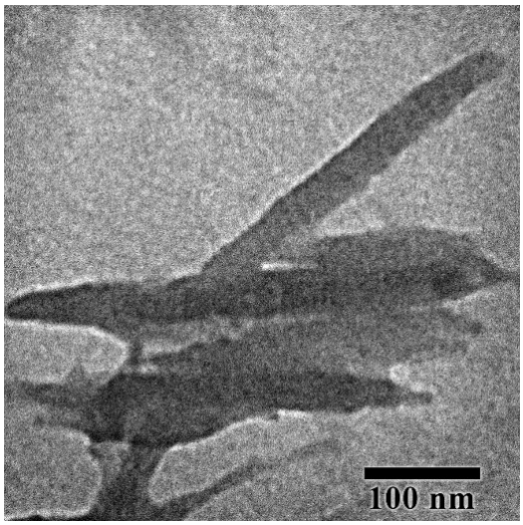

Fig. 1. TEM image of the as-synthesized Ti_3AlC_2 MAX phase in our laboratory.

wear and good self-lubricity were achieved for TiAl materials by the addition of Cu-coated graphite. Such a superior tribological characteristic was related to the synergetic influences of formation of soft tribo-film and hard TiC reinforcement [20].

Beside the metals, ceramic additives can be used as reinforcement to strengthen the TiAl-based materials, in other words, via the development of TiAl matrix composites. For instance, remarkable enhancement in the compression strength of TiAl-based composites, sintered by hot pressing, was observed by the addition of nano-sized TiB_2 ceramic. Simultaneous improvement in ductility and strength of TiAl intermetallics was achieved by the introduction of nano-sized Ti_5Si_3 compound [21]. Increased densification and mechanical performance in TiAl materials was also reported through TiB_2 reinforcing that in-situ synthesized by self-propagating high-temperature synthesis methodology [22]. Addition of nano-sized Y_2O_3

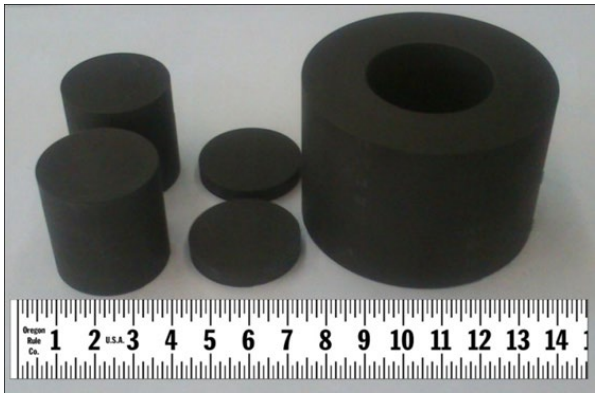

Fig. 2. The graphite die and pistons used for spark plasma sintering of TiAl–Ti_3AlC_2 composites.

led to enhanced tensile strength and elongation in spark plasma sintered high-Nb containing TiAl intermetallics, due to the activation of second-phase strengthening and fine-grain strengthening mechanisms [23].

Beside the ceramics and metals, MAX phases such as Ti_2AlC are also appropriate additives for TiAl materials because of the closeness of their thermal expansion coefficients and specific weights. It should be mentioned that MAX phases have layered structures with combination of both ceramic and metallic properties [24, 25]. The TiAl–Ti_2AlC composites were fabricated by self-propagating high-temperature synthesis [26] and vacuum arc melting [27] using the elemental powders of Ti, Al and C, as well as reactive hot pressing of TiC, Ti and Al powders [28] and spark plasma sintering of mechanically alloyed Al–Ti powders with carbon nanotubes [29].

Recently, a TiAl–15 wt% Ti_3AlC_2 sample was manufactured by our group using spark plasma sintering of Ti, Al and Ti_3AlC_2 powders at 1000 °C for 15 min under 40 MPa [30]. We also synthesized the Ti_3AlC_2 MAX phase in a tubular furnace through self-propagating high-temperature synthesis of elemental powders (graphite as carbon source) [31]. Using such a MAX phase as the reinforcement also led to the performance enhancement in other advanced materials including the ultrahigh temperature ceramics like TiB_2 [32] and ZrB_2 [33].

In this work, five TiAl-based composites doped with 10, 15, 20, 25 and 30 wt% Ti_3AlC_2 MAX phase additive were densified by spark plasma sintering at 900 °C for 7 min under 40 MPa. Displacement-time-temperature variations during the sintering of TiAl–Ti_3AlC_2 composites, displacement rates as the function of temperature/time and densification behavior of the TiAl-based composites versus the amount of Ti_3AlC_2 additive are studied in this paper as the first part of a series of publications. Subsequent parts devoted to phase analysis, mechanical properties, microstructure evolution, and fractographical characterizations will be published in the near future.

2. Experimental procedure

The as-purchased Ti and Al as well as the as-synthesized Ti_3AlC_2 powders were used as starting materials for fabrication of TiAl–Ti_3AlC_2 composites. Titanium and aluminum were selected with equal molar ratios to react with each other to form the in-situ matrix phase of TiAl. The Ti_3AlC_2 compound, previously prepared in our laboratory [31] by the mechanically activated self-propagating high-temperature synthesis method through ball-milling (Retsch PM100) the titanium, aluminum and graphite raw materials for 1 h (please see Fig. 1), was added as the reinforcement to the powder mixtures. The technical characteristics of all as-purchased materials are reported in Table 1.

The values of 10, 15, 20, 25 and 30 wt% Ti_3AlC_2 were selected in the composition of raw materials to fabricate five TiAl-based composite samples. Each powder mixture was ball-milled at a speed of 300 rpm for 1 h.

The powder mixture prepared for the sintering of each sample was calculated to be about 18 g, in order to achieve a final thickness of ~5 mm, and poured into a graphite die with an internal diameter of 30 mm (Fig. 2). It should be noted that to prevent direct contact of powders with the die and pistons, graphite foils with a thickness of 1 mm were used to completely cover the inner surface of the die and the surfaces of the plates. After placing the die filled with the materials, the preliminary pressure applied to the powder mixture was set to a minimum (about 8 MPa).

Table 1. Technical specifications of the as-purchased raw materials.

Powder	Particle size (μm)	Purity (%)	Supplier
Ti	< 40	99.5	Alfa Aesar
Al	< 60	99.0	Fluka
Graphite	< 50	99.5	Merck

Initially, a vacuum of 12–15 Pa was applied and the on-off times of the electrical pulses were set to 2–12; namely, the current was connected for 2 milliseconds and it was cut off for 12 milliseconds. By digitally recording parameters such as the displacement of the furnace mandrels (which can be easily related to the shrinkage of the sample), the instantaneous temperature and the elapsed time, the progress of the sintering process was controlled. Spark plasma sintering was completed at 900 °C under 40 MPa for 7 min for all samples using an SPS furnace (20T-10, China).

Archimedes method was used to calculate the density of sintered samples according to ASTM C 373-88 standard. Each sample was held in boiling water for 5 h and then in distilled water at room temperature for 24 h to measure immersed weight (W_1). After cleaning the surface water from the samples, the wet weight (W_2) was determined. The samples were then placed in a dryer at 110 °C for 12 h and then the dry weight (W_3) was measured. These measurements were repeated three times for each sample. Finally, the bulk density, the relative density, the apparent porosity and the water absorption of the samples were calculated using the following formulas.

$$\rho_b = \frac{W_3}{W_2 - W_1} \quad (1)$$

$$\mathrm{RD}\ (\%) = \frac{\rho_b}{\rho_{th}} \times 100 \quad (2)$$

$$\mathrm{P}\ (\%) = \frac{W_2 - W_3}{W_2 - W_1} \times 100 \quad (3)$$

$$\mathrm{WA}\ (\%) = \frac{W_2 - W_3}{W_3} \times 100 \quad (4)$$

where ρ_b is the bulk density, ρ_{th} is the theoretical density, RD stands for the relative density, P stands for the porosity, and WA stands for the water absorption.

3. Results and discussion

After removing the sintered samples from the graphite die, grinding operation was used to remove the graphite foils attached to the specimens. Images of the sintered samples are presented in Fig. 3. The appearance of all five samples is without macroscopic defects or voids.

Fig. 4 shows the displacement-time-temperature (DTT) diagrams for all five composites made by the spark plasma sintering method, which display the temperature changes as well as the amount of shrinkage in the samples over time.

As can be seen in Fig. 4, in the temperature variation curves, two changes can be detected in the diagrams. The first change is seen at the temperature of about 400 °C, 16 minutes after the start of the heating process, which can be due to the melting of aluminum at the beginning of the process. It should be noted that the melting temperature of aluminum is 660 °C but the temperature specified in the diagram, recorded by the thermocouple (an infrared sensor) located outside of the die, is different from the actual temperature inside the die and between the powder particles. Due to instantaneous plasma sparks, the local temperature between the particles in SPS method is much higher than the temperature measured by the thermocouple [34, 35]. At 400 °C, the temperature rise slope suddenly increases to the final temperature of 900 °C. The reason for this phenomenon is directly related to the beginning of the formation reaction of TiAl matrix, which is extremely exothermic. In addition, another exothermic reaction occurs simultaneously between the matrix phase and the lateral phase of TiC formed as a byproduct during the synthesis of Ti_3AlC_2. Such reaction leads to the production of Ti_2AlC MAX phase. The formation of this compound is also exothermic, which results in a sharp rise in temperature after 400 °C.

Regarding the shrinkage of the specimens, as can be seen, the amount of shrinkage increases with a gentle slope up to 16 min and the specimen shrinks by about 1 mm. The aluminum then melts and the sample shrinks by another 3 mm. Subsequently, no compaction is seen in the samples until after about 35 min, the contraction suddenly increases from 4.5 to 5 mm, which is a sudden increase in the contraction curve due to the sintering progression and the simultaneous application of the final pressure. Finally, another compaction of about 0.5 mm occurs so that the total shrinkage of the samples reaches about 5.5 to 6 mm.

Derivatives of DTT diagrams were used to accurately determine the temperature and time of synthesis and to interpret the sintering process more precisely. Thus, the graphs of displacement rate as a function of temperature (Fig. 5) and displacement rate as a function of time (Fig. 6) for five TiAl–Ti_3AlC_2 composites were also drawn.

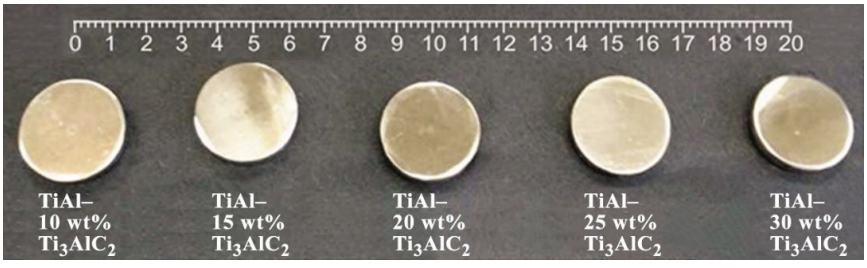

Fig. 3. Five spark plasma sintered TiAl-based samples with different amounts of Ti_3AlC_2 additives.

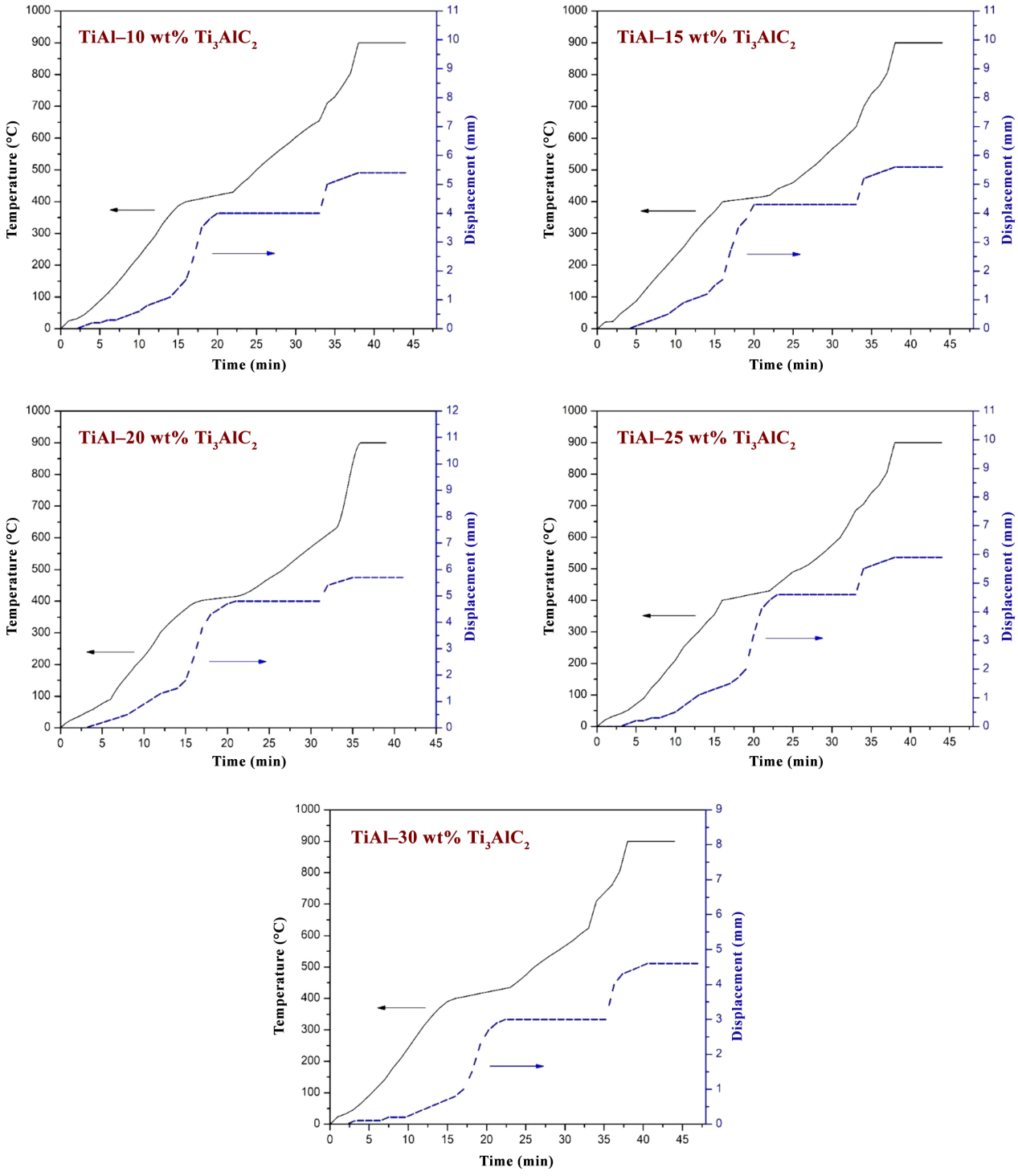

Fig. 4. Displacement-time-temperature variations during the SPS of TiAl–Ti_3AlC_2 composites.

A sharp peak and a few slight peaks are shown in all displacement rate vs. temperature graphs shown in Fig. 5. The main peak, which is larger and more distinct, occurs at a temperature of about 400 °C, which may be related to the melting of aluminum. This phenomenon drastically changes the amount of mandrel displacement and appears in the chart as a sharp peak. At temperatures between 400 and 700 °C, no specific peak is observed, which is probably related to the reactions of TiAl matrix formation and synthesis of Ti_2AlC due to the reaction between the TiAl matrix with TiC phase alongside main Ti_3AlC_2 additive. The slight peak that occurs at a temperature of about 700 °C is due to the

Table 2. Bulk density, apparent porosity, and water absorption of the SPSed TiAl–Ti_3AlC_2 samples.

Sample no.	Ti_3AlC_2 content (wt%)	Bulk density (g/cm^3)	Apparent porosity (%)	Water absorption (%)
1	10	3.72 ± 0.02	4.59	1.2
2	15	3.72 ± 0.01	4.14	1.1
3	20	3.73 ± 0.01	4.07	1.1
4	25	3.74 ± 0.06	4.03	1.1
5	30	3.65 ± 0.02	5.07	1.3

application of final pressure at this temperature, which leads to the displacement of the mandrels and greater compaction of the samples, and helps the part to approach near full density.

In the displacement rate diagram as a function of time (Fig. 6), two sharp peaks and a few initial slight peaks can be identified. The initial weak peaks, which appear in about 4 and 10 minutes, are related to the rearrangement of the powder particles due to the initial applied pressure. The first sharp peak, seen between 15 and 20 minutes, is due to the melting process of aluminum. There is no specific peak in the curves between 22 and 32 minutes, which is probably related to the dissolution of titanium particles in molten aluminum and the formation of the TiAl matrix. Also, a reaction between TiC (byproduct of the as-synthesized Ti_3AlC_2 additive) and the in-situ synthesized TiAl matrix occurs and the Ti_2AlC MAX phase is formed. Finally, another sharp peak is seen before the 35th min, which is related to the final applied pressure and leads to the densification of the parts.

The results of measurements and calculations of bulk density, apparent porosity and water absorption of all five sintered TiAl–Ti_3AlC_2 composite samples are reported in Table 2. Fig. 7 also shows the

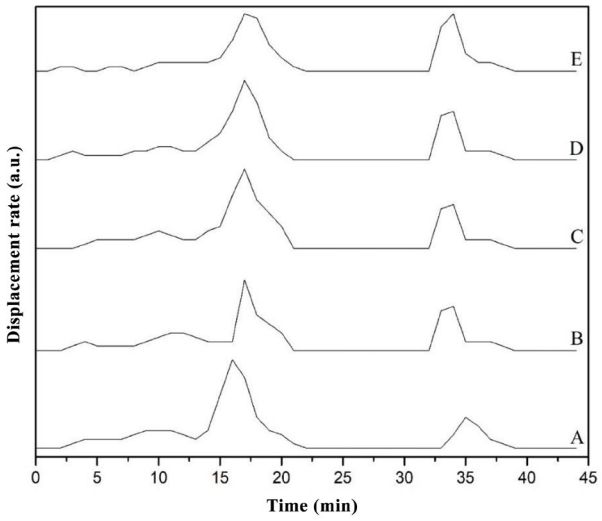

Fig. 6. Displacement rate as a function of time for A: TiAl–10 wt% Ti_3AlC_2, B: TiAl–15 wt% Ti_3AlC_2, C: TiAl–20 wt% Ti_3AlC_2, D: TiAl–25 wt% Ti_3AlC_2, and E: TiAl–30 wt% Ti_3AlC_2 composites.

relative density variations as a function of the amount of Ti_3AlC_2 MAX phase additive. According to the values obtained from the relative density calculations, it is clear that the best results are related to the samples containing 20 and 25 wt% additives. The worst result is for the sample reinforced with 30 wt% of Ti_3AlC_2 additive. As presented in Table 2, the addition of Ti_3AlC_2 (to 25 wt%) reduces the apparent porosity because the MAX phase, as a sintering aid, helps to improve the densification of the material. Higher amounts of Ti_3AlC_2 appear to have the negative effect via increasing the amount of apparent porosity, which leads to a decrease in relative density, perhaps due to agglomeration of the MAX phase particles.

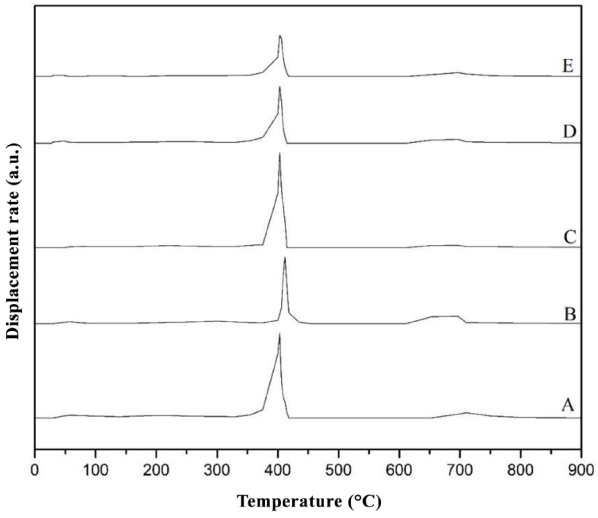

Fig. 5. Displacement rate as a function of temperature for A: TiAl–10 wt% Ti_3AlC_2, B: TiAl–15 wt% Ti_3AlC_2, C: TiAl–20 wt% Ti_3AlC_2, D: TiAl–25 wt% Ti_3AlC_2, and E: TiAl–30 wt% Ti_3AlC_2 composites.

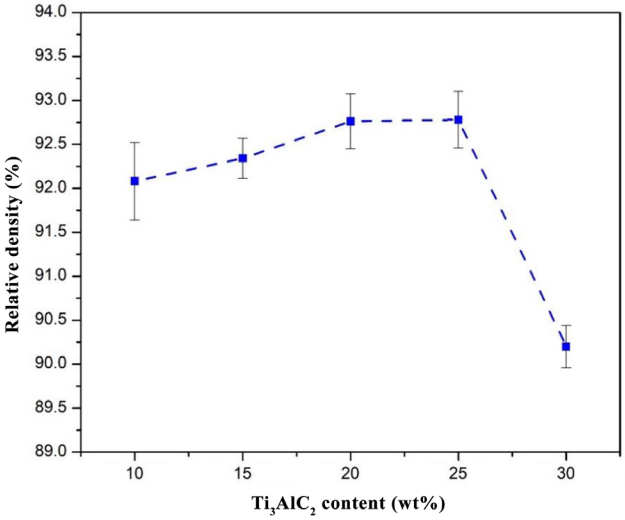

Fig. 7. Relative density of the as-sintered TiAl-based composites as a function of amount of Ti_3AlC_2 additive.

4. Conclusions

Role of various amounts of Ti_3AlC_2 MAX additive (10, 15, 20, 25 and 30 wt%) on the spark plasma sinterability of TiAl matrix composites was investigated. Sintering by SPS route was performed in vacuum atmosphere at 900 °C for 7 min under 40 MPa using the ball-milled metallic Ti and Al particulates with the self-synthesized Ti_3AlC_2 MAX phase. Displacement-time-temperature variations in the heating and sintering steps, as well as displacement rates versus temperature and time were plotted. Two remarkable changes were observed in the diagrams: (1) due to the melting of Al after ~16 min, and (2) because of the final applied load and the sintering progression after ~35 min. Densification progression in terms of the bulk density, the relative density, the apparent porosity, and the water absorption were studied and compared. The highest relative density was achieved by the addition of 20 or 25 wt% Ti_3AlC_2.

CRediT authorship contribution statement

Maryam Akhlaghi: Investigation, Data curation, Writing – original draft, Visualization.
Esmaeil Salahi: Project administration, Supervision, Methodology.
Seyed Ali Tayebifard: Conceptualization, Funding acquisition, Validation.
Gert Schmidt: Writing – review & editing.

Data availability

The data underlying this article will be shared on reasonable request to the corresponding author.

Declaration of competing interest

The authors declare no competing interests.

Funding and acknowledgment

The content of this article is based on the PhD thesis of the first author. The authors would like to express their gratitude to the Materials and Energy Research Center for its support of this research project under grant number 481394051. Additionally, the invaluable assistance of Dr. Behzad Nayebi in result analysis and Mrs. Masoumeh Enayati and Mrs. Nadi Shojaei in conducting the experiments is sincerely appreciated.

References

[1] Z. Duan, Y. Han, X. Song, H. Chen, Creep behaviour of equiaxed fine-grain γ-TiAl-based alloy prepared by powder metallurgy, Mater. Sci. Technol. 36 (2020) 1457–1464. https://doi.org/10.1080/02670836.2020.1790098.
[2] H.P. Lim, W.Y.H. Liew, G.J.H. Melvin, Z.-T. Jiang, A Short Review on the Phase Structures, Oxidation Kinetics, and Mechanical Properties of Complex Ti-Al Alloys, Materials (Basel). 14 (2021) 1677. https://doi.org/10.3390/ma14071677.
[3] H. Huang, H. Ding, X. Xu, R. Chen, J. Guo, H. Fu, Phase transformation and microstructure evolution of a beta-solidified gamma-TiAl alloy, J. Alloys Compd. 860 (2021) 158082. https://doi.org/10.1016/j.jallcom.2020.158082.
[4] M.-P. Bacos, S. Ceccacci, J.-P. Monchoux, C. Davoine, T. Gheno, et al., Oxidation Behavior of a Spark Plasma Sintered Ti–48Al–2W–0.1B Alloy at 800 °C, Oxid. Met. 93 (2020) 587–600. https://doi.org/10.1007/s11085-020-09973-8.
[5] Y. Jiang, Y. He, H. Gao, Recent progress in porous intermetallics: Synthesis mechanism, pore structure, and material properties, J. Mater. Sci. Technol. 74 (2021) 89–104. https://doi.org/10.1016/j.jmst.2020.10.007.
[6] Z. Trzaska, G. Bonnefont, G. Fantozzi, J.-P. Monchoux, Comparison of densification kinetics of a TiAl powder by spark plasma sintering and hot pressing, Acta Mater. 135 (2017) 1–13. https://doi.org/10.1016/j.actamat.2017.06.004.
[7] G.H. Cao, A.M. Russell, C.-G. Oertel, W. Skrotzki, Microstructural evolution of TiAl-based alloys deformed by high-pressure torsion, Acta Mater. 98 (2015) 103–112. https://doi.org/10.1016/j.actamat.2015.07.012.
[8] C.Y. Teng, N. Zhou, Y. Wang, D.S. Xu, A. Du, et al., Phase-field simulation of twin boundary fractions in fully lamellar TiAl alloys, Acta Mater. 60 (2012) 6372–6381. https://doi.org/10.1016/j.actamat.2012.08.016.
[9] Y. Garip, Investigation of isothermal oxidation performance of TiAl alloys sintered by different processing methods, Intermetallics. 127 (2020) 106985. https://doi.org/10.1016/j.intermet.2020.106985.
[10] J. Shen, L. Hu, L. Zhang, W. Liu, A. Fang, Y. Sun, Synthesis of TiAl/Nb composites with concurrently enhanced strength and plasticity by powder metallurgy, Mater. Sci. Eng. A. 795 (2020) 139997. https://doi.org/10.1016/j.msea.2020.139997.
[11] Z.-Y. Hu, Z.-H. Zhang, X.-W. Cheng, F.-C. Wang, Y.-F. Zhang, S.-L. Li, A review of multi-physical fields induced phenomena and effects in spark plasma sintering: Fundamentals and applications, Mater. Des. 191 (2020) 108662. https://doi.org/10.1016/j.matdes.2020.108662.
[12] N.F. Mogale, W.R. Matizamhuka, Spark Plasma Sintering of Titanium Aluminides: A Progress Review on Processing, Structure-Property Relations, Alloy Development and Challenges, Metals (Basel). 10 (2020) 1080. https://doi.org/10.3390/met10081080.
[13] M. Musi, B. Galy, J.-P. Monchoux, A. Couret, H. Clemens, S. Mayer, In-situ observation of the phase evolution during an electromagnetic-assisted sintering experiment of an intermetallic γ-TiAl based alloy, Scr. Mater. 206 (2022) 114233. https://doi.org/10.1016/j.scriptamat.2021.114233.
[14] D. Wimler, J. Lindemann, T. Kremmer, H. Clemens, S. Mayer, Microstructure and mechanical properties of novel TiAl alloys tailored via phase and precipitate morphology, Intermetallics. 138 (2021) 107316. https://doi.org/10.1016/j.intermet.2021.107316.
[15] Y. Su, Y. Lin, N. Zhang, D. Zhang, Microstructures and mechanical properties of TiAl alloy fabricated by spark plasma sintering, Int. J. Mod. Phys. B. 34 (2020) 2040036. https://doi.org/10.1142/S0217979220400366.
[16] E. Hug, G. Dirras, News Trends in Powder Metallurgy: Microstructures, Properties, Durability, Metals. 11 (2021) 1216. https://doi.org/10.3390/met11081216.
[17] S. Shu, F. Qiu, C. Tong, X. Shan, Q. Jiang, Effects of Fe, Co and Ni elements on the ductility of TiAl alloy, J. Alloys Compd. 617 (2014) 302–305. https://doi.org/10.1016/j.jallcom.2014.07.199.
[18] X. Gu, F. Cao, N. Liu, G. Zhang, D. Yang, et al., Microstructural evolution and mechanical properties of a high yttrium containing TiAl based alloy densified by spark plasma sintering, J. Alloys Compd. 819 (2020) 153264. https://doi.org/10.1016/j.jallcom.2019.153264.
[19] P.V. Cobbinah, W. Matizamhuka, R. Machaka, M.B. Shongwe, Y. Yamabe-Mitarai, The effect of Ta additions on the oxidation resistance of SPS-produced TiAl alloys, Int. J. Adv. Manuf. Technol. 106 (2020) 3203–3215. https://doi.org/10.1007/s00170-019-04885-7.
[20] L. Wang, A.K. Tieu, Q. Zhu, J. Chen, J. Cheng, et al., Achieving the excellent self-lubricity and low wear of TiAl intermetallics through the addition of copper coated graphite, Compos. Part B: Eng. 198 (2020) 108223. https://doi.org/10.1016/j.compositesb.2020.108223.

[21] S. Shu, B. Xing, F. Qiu, S. Jin, Q. Jiang, Comparative study of the compression properties of TiAl matrix composites reinforced with nano-TiB2 and nano-Ti5Si3 particles, Mater. Sci. Eng. A. 560 (2013) 596–600. https://doi.org/10.1016/j.msea.2012.10.001.
[22] C.L. Yeh, S.H. Su, In situ formation of TiAl–TiB2 composite by SHS, J. Alloys Compd. 407 (2006) 150–156. https://doi.org/10.1016/j.jallcom.2005.06.053.
[23] Y. Guo, Y. Liang, J. Lin, F. Yang, Effect of Nano-Y2O3 Addition on Microstructure and Tensile Properties of High-Nb TiAl Alloy Prepared by Spark Plasma Sintering, Metals (Basel). 11 (2021) 1048. https://doi.org/10.3390/met11071048.
[24] M. Radovic, M.W. Barsoum, MAX phases: bridging the gap between metals and ceramics, Am. Ceram. Soc. Bull. 92 (2013) 20–27.
[25] X.H. Wang, Y.C. Zhou, Layered Machinable and Electrically Conductive Ti2AlC and Ti3AlC2 Ceramics: a Review, J. Mater. Sci. Technol. 26 (2010) 385–416. https://doi.org/10.1016/S1005-0302(10)60064-3.
[26] C.L. Yeh, Y.G. Shen, Formation of TiAl–Ti2AlC in situ composites by combustion synthesis, Intermetallics. 17 (2009) 169–173. https://doi.org/10.1016/j.intermet.2008.10.014.
[27] X.-J. Song, H.-Z. Cui, N. Hou, N. Wei, Y. Han, et al., Lamellar structure and effect of Ti2AlC on properties of prepared in-situ TiAl matrix composites, Ceram. Int. 42 (2016) 13586–13592. https://doi.org/10.1016/j.ceramint.2016.05.152.
[28] C. Yang, F. Wang, T. Ai, J. Zhu, Microstructure and mechanical properties of in situ TiAl/Ti2AlC composites prepared by reactive hot pressing, Ceram. Int. 40 (2014) 8165–8171. https://doi.org/10.1016/j.ceramint.2014.01.012.
[29] F. Yang, F.T. Kong, Y.Y. Chen, S.L. Xiao, Effect of spark plasma sintering temperature on the microstructure and mechanical properties of a Ti2AlC/TiAl composite, J. Alloys Compd. 496 (2010) 462–466. https://doi.org/10.1016/j.jallcom.2010.02.077.
[30] M. Akhlaghi, S.A. Tayebifard, E. Salahi, M. Shahedi Asl, Spark plasma sintering of TiAl–Ti3AlC2 composite, Ceram. Int. 44 (2018) 21759–21764. https://doi.org/10.1016/j.ceramint.2018.08.272.
[31] M. Akhlaghi, S.A. Tayebifard, E. Salahi, M. Shahedi Asl, G. Schmidt, Self-propagating high-temperature synthesis of Ti3AlC2 MAX phase from mechanically-activated Ti/Al/graphite powder mixture, Ceram. Int. 44 (2018) 9671–9678. https://doi.org/10.1016/j.ceramint.2018.02.195.
[32] B. Nayebi, M. Shahedi Asl, M. Akhlaghi, Z. Ahmadi, S.A. Tayebifard, et al., Spark plasma sintering of TiB2-based ceramics with Ti3AlC2, Ceram. Int. 47 (2021) 11929–11934. https://doi.org/10.1016/j.ceramint.2021.01.033.
[33] M. Shahedi Asl, B. Nayebi, M. Akhlaghi, Z. Ahmadi, S.A. Tayebifard, et al., A novel ZrB2-based composite manufactured with Ti3AlC2 additive, Ceram. Int. 47 (2020) 817–827. https://doi.org/10.1016/j.ceramint.2020.08.193.
[34] F. Sadegh Moghanlou, M. Vajdi, M. Sakkaki, S. Azizi, Effect of graphite die geometry on energy consumption during spark plasma sintering of zirconium diboride, Synth. Sinter. 1 (2021) 54–61. https://doi.org/10.53063/synsint.2021.117.
[35] S. Jafargholinejad, S. Soleymani, Effects of carbon nano-additives on characteristics of TiC ceramics prepared by field-assisted sintering, Synth. Sinter. 1 (2021) 62–68. https://doi.org/10.53063/synsint.2021.1123.